

Shell-model and first-principles calculations of vibrational, structural and ferroelectric properties of KH_2PO_4

R. E. Menchón , F. Torresi , J. Lasave , S. Koval *

Instituto de Física Rosario, Universidad Nacional de Rosario and CONICET, 27 de Febrero 210 Bis, 2000 Rosario, Argentina

Received July 07, 2022, in final form August 12, 2022

We develop a shell model (SM) for potassium dihydrogen phosphate (KDP) which is fitted to *ab initio* (AI) results that include nonlocal van der Waals corrections. The SM is comprehensively tested by comparing results of structural, vibrational and ferroelectric properties with AI and experimental data. The relaxed structural parameters are in very good agreement with the AI results and the available experimental data. The Γ -point phonons and the total phonon densities of states (DOSs) in the ferroelectric and paraelectric phases calculated with the developed SM are in good overall agreement with the corresponding AI and experimental data. We also compute the effective Debye temperature as a function of T which shows good accordance with the corresponding AI and experimental results. Classical molecular dynamics (MD) simulations obtained with the developed SM show a FE-PE phase transition at ≈ 360 K in remarkable agreement with *ab initio* MD calculations.

Key words: *ferroelectrics, hydrogen bonds, phase transitions, shell model, density functional theory*

1. Introduction

The prototype of the H-bonded ferroelectric (FE) compounds, KH_2PO_4 or KDP, was extensively studied in the past due to its important technological applications as well as for fundamental interest in its phenomenology [1]. In subsequent years after its discovery, KDP found extensive applications as electro-optical devices, as well as filter modulators in the wide field of laser spectroscopy. Besides the research in technological aspects, many efforts were also directed in the past to unveil the puzzle in the origin of the huge isotope effect that KDP manifests: the critical temperature T_c for the paraelectric-ferroelectric (PE-FE) phase transition nearly doubles when the system is deuterated [2, 3]. In spite of these efforts, the controversy about whether tunneling [4, 5] or geometrical effects [2, 3] are at the root of the giant isotope effect still remains.

This phenomenology is widely observed in the whole family of H-bonded ferroelectric compounds [6–13] including organic ferroelectrics that were recently discovered which attract much attention because of their potential for ecofriendly technological applications [14, 15]. *Ab initio* (AI) calculations have shown that tunneling and geometrical effects are involved in a self-consistent phenomenon that greatly amplifies the effect of their correlation leading to the huge isotope effect observed [7, 16].

With the aim of studying the phase transition and the isotope effects in KDP, many models were developed in the past [4, 6, 17–20], e.g., the tunneling model and subsequent modifications [4, 6, 17, 18]. The coupled proton-phonon model, which accounts for the interaction between the proton collective mode exhibiting tunneling and the optical lattice phonon of B_2 symmetry polarized along the z -axis, was invoked to explain the emergence of polarization in the z -direction [17, 18]. The lower-frequency mode arising from this interaction is the FE soft mode that softens with temperature when the critical temperature is approached. Infrared measurements have also shown strong correlations between these

*Corresponding author: koval@ifir-conicet.gov.ar.

modes and an overdamped internal mode ν_4 related to a quadrupole distortion of the phosphates [21]. Recent AI calculations have confirmed the strong couplings of the FE soft mode with the lattice B_2 phonon and the internal ν_4 mode, as well as predicted important correlations with the phosphate libration mode of A_1 symmetry [22]. The latter could be relevant to the geometrical effect observed because phosphate librations are associated with a change in the H-bond geometry.

Recently AI calculations were successfully used to study phonons and vibrational properties in H-bonded FE compounds [13, 22]. However, generally, the AI approach is not computationally feasible when dealing with dynamical calculations in large-size systems to simulate the phase transition near T_c , where long-range effective interactions are essential. Even more demanding would be to simultaneously describe the quantum nature of protons or deuterons, e.g., via path integral simulations, although some AI calculations including nuclear quantum effects were recently performed but with the focus on the PE phase properties rather than on the phase transition itself [24, 25]. Moreover, the development of a SM adjusted to AI results yielding reliable and transferable interatomic potential parameters, especially for the H-bond unit, could be useful to undertake calculations on complex systems like some organic FE materials [14].

In spite of their importance, lattice dynamics studies with atomistic models in H-bonded ferroelectrics like KDP were remarkably scarce in the past [26–28]. These studies could be very useful to provide reliable interatomic potential parameters in order to perform atomistic simulations for the study of the FE phase transitions that these materials exhibit. On the other hand, due to the lack of confident microscopic information, many models developed in the past for these systems were validated *a posteriori* on the basis of their predictions. For example, indications of the existence of tunneling were recently reported by Compton neutron scattering experiments [5], many decades after the development of the tunneling model and its modifications. With the advent of the electronic structure calculations based on the DFT theory, we have now the possibility of tuning the parameters of a model to reproduce microscopic details of the system obtained from first principles. Thus, it is desirable to develop an atomistic model adjusted to confident AI results.

A preliminary atomistic shell model (SM) for KDP [29, 30] was fitted to AI results obtained with the PBE-GGA functional [7, 16]. A SM was chosen for the atomistic description of the system because this kind of models was successful in describing the large oxygen polarization in related systems such as ferroelectric perovskites [31] or other oxide materials [32–36]. The work of reference [29] represents a first step towards the development of a reliable atomistic model necessary for the study of the phase transition with simulations of large-size systems. However, the fit yielded a rather contracted geometry for the H-bonds and small values for the basal lattice parameters compared to the experiment. This is due to the fact that the model was fitted to the results from PBE calculations which, due to the neglect of the van der Waals (vdW) interactions, underestimate the O–O distances and the energy-barriers for the polarization-inversion [10, 22, 37]. For instance, the energy barriers obtained at the PBE level [29] are of the order of ≈ 4 to 5 times and ≈ 10 times smaller than those calculated with the non-local vdW-DF approach and the Möller-Plesset second order perturbation theory (MP2), respectively [22]. Similarly, the PBE results for the O–O distance and the parameter δ , which is twice the proton distance to the middle of the O–H–O bond, appears $\approx 4\%$ and $\approx 50\%$ smaller, respectively, than the corresponding values of both, the vdW-DF and MP2 methods [22]. We remark here that the approximate inclusion of nuclear quantum effects [10, 22] for the PBE results lead to an important disagreement with the experiment for the last mentioned magnitudes, especially the equilibrium proton distance δ which appears to be too short: 0.015 Å compared to 0.385 Å for the experimental value [22]. On the other hand, nuclear quantum corrections (NQC) applied to the vdW-DF case lead to a value of $\delta = 0.355$ Å, in excellent agreement with the experiment [22]. The high-energy phonons related to the H-bond dynamics have also much smaller frequencies in the PBE scheme than those obtained with nonlocal vdW approaches such as the vdW-DF method [22, 38]. We conclude that the SM developed in reference [29] would not be suitable for describing correctly the phase transition due to the resulting contracted H-bond geometry and the small global proton-transfer energy barriers.

In this work, we have developed a new SM based on interatomic potentials by adjusting its parameters to old and new AI structural data that include vdW corrections using the so-called vdW-DF approach, which had the best performance among different AI methods to reproduce experimental structural and vibrational properties of KDP and DKDP [22]. The developed SM, together with new AI calculations, were

used to study different ferroelectric, structural and vibrational properties. The SM calculations included full structural relaxations, zone-center phonons, phonon densities of states, the effective Debye temperature and a “classical-nuclei” SM molecular dynamics study of the phase transition which were compared to AI molecular dynamics simulations also performed here. In this paper we have also determined new full structural AI relaxations in the PE and FE phases, and computed the AI total phonon density of states in the PE phase. These data together with previous AI data from reference [22] and available experimental results were used to extensively test the results of the new model developed. The SM results for the effective Debye temperature show good agreement compared to AI [22] and experimental data. Moreover, we have found a very good agreement in the results of the SM and AI molecular dynamics simulations performed for the study of the phase transition in deuterated KDP (DKDP).

This paper is organized as follows: in section 2 we give details about the SM developed and the AI and SM calculations performed. The results are presented in section 3. In the first subsection 3.1 we analyze the structures obtained with the present SM for the PE and FE phases and compare them with AI (vdW-DF) results as well as with the available experimental data. The SM calculations of the phonons and related properties are presented in section 3.2, which are in turn divided into two subsections. In the first subsection 3.2.1 we report some of the SM phonons at the Brillouin zone center and compare them with AI and experimental data. Besides, we also present a comparison of the total DOS in the FE and PE phases with the corresponding AI results. In the second subsection 3.2.2, we analyze the SM results for the effective Debye temperature and compare them with the corresponding AI and experimental data. In section 3.3 we present molecular dynamics simulations for the developed SM and compare them with AI results. Finally, a summary is presented in section 4.

2. Shell model and *ab initio* methods. Calculation details

The PE phase of KDP has a body-centered tetragonal bct structure with shorter lattice constant along the tetragonal axis. The space group is $I\bar{4}2d$ or D_{2d}^{12} . In the FE phase, the crystal is 0.8% shear distorted along the $[110]$ direction and becomes orthorhombic with space group $Fdd2$ or C_{2v}^{19} . The primitive cell in both phases contains 16 atoms (two formula units).

In the PE phase of KDP, the hydrogens have two equilibrium positions equidistant to the middle of the O–H–O bond and separated by a distance δ . Both positions are occupied by these protons with equal probability in this phase, and hence the averaged proton position is $\langle x \rangle = \langle \delta \rangle / 2 = 0$. Therefore, in the AI and SM simulations for this phase, we performed full structural optimizations with the H atoms exactly at the middle of the O–H–O bonds [13], which remained in their positions after relaxations due to symmetry reasons. This hypothetical phase at 0 K is used to keep the macroscopic center inversion symmetry of $I\bar{4}2d$ phase. For this phase, the phonon calculations give three unstable modes of imaginary frequency, one of which is shown in table 3. In the case of the FE phase, the protons are originally slightly displaced from the middle of the O–H–O bonds following the pattern of the FE mode. After that, the full structural SM and AI relaxations lead the system in each case to the ordered FE phase. In the SM and AI optimized-cell structural relaxations for both phases, the cell plus atomic structural parameters were allowed to relax at zero pressure.

Our starting point for the SM is the one developed in reference [29]. It contains ionic polarizabilities for the P and O ions which are described by an electronic shell with charge Y harmonically coupled with a spring k_{sc} to the core. In addition, we consider short-range shell-shell repulsive interactions arising from the wavefunction overlap between neighboring ions and long-range Coulomb interactions between cores and shells of every ion. The short-range interactions are of the Born–Mayer type, $Ae^{-r/\rho}$, for the P–O and O–H bonds as well as of the Buckingham type, $Ae^{-r/\rho} - C/r^6$, for the K–O bonds [32, 33, 36]. Three-body angular potentials of the form $(1/2)k(\theta - \theta_0)^2$ for the covalent O–P–O and P–O–H bonds [36] and a three-body potential represented by the term $(D/r^{12} - B/r^{10}) \cos^4(\theta - 180^\circ)$ for the O–H–O bond are also included [29]. Considering the total charge Z of the ions and using the condition of charge neutrality, the model finally contains 20 adjustable parameters.

The SM simulations were carried out using the GULP code [39] which can perform structure optimizations at zero temperature as well as phonon calculations (phonon frequencies and eigenvectors at the Brillouin zone center, phonon dispersion curves and density of states, etc.) and classical molecular

Table 1. Shell model parameters for the present work.

	H _{core}	O _{core}	P _{core}	K _{core}	O _{shell}	P _{shell}
charge [e]	0.65	1.10	4.80	0.60	-2.40	-1.50

Two-Body Potentials				Three-Body Potentials		
harmonic	k_{sc} [eV Å ⁻²]			angular harmonic	k [eV rad ⁻²]	θ_0 [°]
O _{core} -O _{shell}	68.0			O _{core} -P _{core} -O _{core}	18.00	109.0
P _{core} -P _{shell}	1950.0			H _{core} -O _{core} -P _{core}	2.75	115.8
Buckingham	A [eV]	ρ [Å]	C [eV Å ⁶]	hydrogen bond 12-10-4	D [eV Å ¹²]	B [eV Å ¹⁰]
H _{core} -O _{shell}	184.5	0.21	0.0	O _{core} -H _{core} -O _{core}	20478.0	1750.0
O _{shell} -P _{shell}	805.0	0.30	0.0			
O _{shell} -K _{core}	5175.0	0.32	507.5			

dynamics simulations.

The AI calculations in the PE and FE phases of KDP were performed with the VASP code using projector augmented wave (PAW) all-electron potentials [40, 41]. The plane-wave basis was expanded to an energy cutoff of 750 eV. In the calculations we use an automatic Monkhorst-Pack $5 \times 5 \times 5$ grid sampling of the electronic Brillouin zone, which proved sufficient to achieve converged results. The calculations were carried out using the AI scheme vdW-DF that includes nonlocal van der Waals dispersion corrections [42–44]. The geometry optimizations were performed until the forces on every atom were smaller than 5 meV/Å.

Shell model molecular dynamics (SMMD) and *ab initio* molecular dynamics (AIMD) simulations were performed in the NVT ensemble with the GULP and VASP programs, respectively, using a Nosé-Hoover thermostat to control the temperature. The Newton's equations of motion were integrated using the Verlet's algorithm with a typical time step of 0.3 fs (0.2 fs) in the AIMD (SMMD) simulations for an accurate integration of the electronic degrees of freedom in H-bonded systems. The AIMD (SMMD) calculations were carried out for a series of temperatures from 200 to 500 K using supercells of 128 (256) atoms subjected to periodic boundary conditions. At each temperature, a well equilibrated configuration is achieved after running at least 5 ps. Then, the system evolves further at least 5 and 15 ps to calculate the thermodynamic averages in the AIMD and SMMD calculations, respectively.

The AIMD calculations were performed with a high-accuracy cutoff energy of 600 eV and Γ -point Brillouin zone sampling, and include nonlocal dispersion corrections at the vdW-DF level. It is worth mentioning that in order to ensure that the energy is well converged we have verified that the drift produced by the Nosé-Hoover dynamics is less than 1 meV/atom within a time step of 1 ps [45].

The lattice parameters were fixed in the simulations for DKDP to those corresponding to the experimental values in the PE phase measured at $T_c + 5$ K \approx 234 K [46]. Accordingly, the ordered phase at low temperature arises in the calculations at fixed cell (NVT ensemble) as a FE phase with tetragonal lattice, which is slightly distorted with respect to the orthorhombic lattice [47]. This strategy enables the study of the phase transition using a supercell that conserves volume. We verified that all AIMD and SMMD simulations yield to average equilibrium structures which are stable up to the largest temperature considered $T = 500$ K.

The total *ab initio* phonon density of states (PDOS) was derived from the phonon calculations using the finite difference (FD) method as implemented in the PHONOPY code [22, 48, 49]. Here, in order to compute the atomic forces for the different configurations generated by the PHONOPY FD method we used the VASP program with the vdW-DF method to account for nonlocal dispersion effects. In this case, the energy cutoff for the plane-wave basis was set to 450 eV, and a $4 \times 4 \times 4$ grid for the Brillouin zone sampling was used. The atomic distortions were performed in a $2 \times 2 \times 2$ supercell with 128 atoms. In this case we used a tighter tolerance in the forces of 0.5 meV/Å in order to achieve convergence in the phonon dispersion results. Once the phonon dispersion relations were obtained, the PHONOPY code allowed us to calculate the total PDOS by a Brillouin zone integration.

3. Results and discussion

3.1. Structural optimizations

The model parameters of the SM were initially taken from reference [29] and were further adjusted in order to reproduce the AI (vdW-DF) results for the relaxed internal structure and lattice constants in the FE and PE phases. Special emphasis was made on reproducing the O–O distance and the parameter δ for the H-bonds, which were mainly controlled by adjusting the three-body potential for the O–H–O bond and the Born–Mayer O–H potential. Once the set of parameters satisfactorily reproduced the structure of both phases, we further refined the model to adjust better the Brillouin zone-center (Γ -point) phonons to the AI data. In doing this, due to the complexity of the system, special care was taken to adjust various properties at the same time without spoiling the whole fit.

In table 2, we present results of the structural parameters obtained with full AI and SM relaxations (atomic plus cell optimizations) in the PE and FE phases. These results are compared to the corresponding AI values from reference [22]. A good overall agreement between the AI (vdW-DF) and SM structural parameters results for both phases is observed in table 2. Moreover, the comparison of these results with the available experimental data is also satisfactory, with relative percentage differences of the order or less than 3% in most of the cases. The underestimation in the O–O distance in the PE phase can be mainly attributed to the static optimization for centered protons in the H-bonds [7, 16], while in the actual PE phase observed at finite temperature, the protons are delocalized over two symmetric, off-center positions along the bond [2, 3]. Notice that the theoretical calculations correspond to classical (infinite mass) nuclei. Actually, H-bond parameters such as the O–O, O–H and δ distances are especially affected by the quantum dynamics of the proton [10, 22]. The inclusion of these dynamics approximately by means of PIMC calculations, leads to NQC that improve the correspondence of the AI results for these parameters [22] with the experiment. Notice that the present SM calculations overestimate the relaxed H-bond geometry in the FE phase in comparison with the experiment, e.g., the O–O distance and the parameter δ (see table 2). Therefore, due to the fact that NQC produce a contraction in the H-bonds [22], we speculate that if NQC were applied to the SM calculations, the agreement with the experiment for the H-bond geometry could be improved.

Table 2. SM and AI (vdW-DF) results of the lattice and internal structure parameters for the FE and PE phases of KDP. Also shown is the experimental data of reference [46]. Distances in angstroms and angles in degrees. We also show in parenthesis the relative percentage differences with available experimental data.

Structural Parameters	Expt. [46]	FE structure		Expt. [46]	PE structure	
		vdW-DF optimized cell	SM optimized cell		vdW-DF optimized cell	SM optimized cell
a	10.546	10.836 (2.8)	10.893 (3.3)	7.426	7.531 (1.4)	7.258 (2.3)
b	10.466	10.741 (2.6)	10.099 (3.5)			
c	6.927	7.119 (2.8)	6.925 (0.1)	6.931	7.096 (2.4)	6.933 (0.3)
d (O...O)	2.497	2.612 (4.6)	2.585 (3.5)	2.483	2.430 (2.1)	2.429 (2.2)
d (O ₂ –H)	1.056	1.022 (3.2)	0.949 (10)	1.071	1.215 (13)	1.217 (13)
d (H...O ₁)	1.441	1.590 (10)	1.637 (14)	1.412	1.215 (14)	1.217 (14)
δ	0.385	0.568 (48)	0.687 (78)			
\angle (O ₂ –H...O ₁)	179.4	179.8 (0.2)	177.7 (0.9)	178.2	178.5 (0.2)	173.0 (2.9)
d (P...K)	–	3.402	3.384	–	3.548	3.467
d (K...P)	–	3.717	3.542	–	3.548	3.467
d (P–O ₁)	1.516	1.524 (0.5)	1.527 (0.7)			
d (P–O ₂)	1.572	1.617 (2.9)	1.692 (7.6)	1.543	1.564 (1.4)	1.595 (3.4)
d (K...O ₁) (nn)	2.785	2.854 (2.5)	2.707 (2.8)			
d (K...O ₂) (nn)	2.825	2.908 (2.9)	2.730 (3.4)	2.809	2.888 (2.8)	2.672 (4.9)
d (K...O ₁) (nnn)	2.847	2.914 (2.4)	2.811 (1.3)			
d (K...O ₂) (nnn)	2.914	3.011 (3.3)	2.891 (0.8)	2.881	2.952 (2.5)	2.859 (0.8)

3.2. Vibrational properties

3.2.1. Γ -point phonons and density of states

We have checked the capability of the developed SM to reproduce vibrational properties of the system obtained from first principles calculations. To this end, we compare some of the SM Brillouin zone-center phonons with the corresponding AI (vdW-DF) and experimental data in table 3. The table is organized in view of the correspondence between representations in the PE and FE phases. [22] Therefore, frequencies in the same row correspond to qualitatively similar patterns of motion for both phases, although the correspondence should be taken with caution because in some cases there were ambiguities in the assignment. In table 3, we show the SM results for the zone-center phonons of symmetry A_1 , A_2 , B_1 , and B_2 in the PE phase, which are divided into the two subspaces, $(A_1 + B_2)$ and $(A_2 + B_1)$. In the right-hand panel we report the corresponding SM frequencies of the A_1 and A_2 modes in the FE phase.

Table 3. SM results of the Γ -point phonons of symmetries A_1 , B_2 , A_2 , B_1 (PE phase) and A_1 , A_2 (FE phase) for KDP. Also shown are the AI (VASP) results obtained with the exchange-correlation functional vdW-DF from reference [22] and the experimental results of references [50–52] for the PE phase and references [21, 50, 53] for the FE phase. The phonon frequencies are shown in cm^{-1} . According to the calculated eigenvectors, the following classification is shown in the table: ferroelectric unstable mode with imaginary frequency (FE), external translational (ET), external rotational (ER), internal molecular P–O bending (IMB), internal molecular P–O stretching (IMS), O–H . . . O bending (HB), and O–H . . . O stretching (HS).

PE structure							FE structure						
Sym.	SM	vdW-DF [22]	Expt. [50]	Expt. [51]	Expt. [52]	Class.	Sym.	SM	vdW-DF [22]	Expt. [50]	Expt. [53]	Expt. [21]	Class.
B_2	1096i	819i				FE, HS + IMB	A_1	2528	2600				HS
B_2	226	189	180	180	179.5	ET	A_1	227	185	185	142	209	ET
A_1	648	543			520.3	IMB	A_1	274	257		283		IMB
A_1	422	295	360	363	363.9	IMB	A_1	528	345	346	369		IMB
B_2	610	391	395	393	394.0	IMB	A_1	595	383	394	393		IMB
B_2	593	533				IMB	A_1	623	488	515			IMB
A_1	784	917	915		916.9	IMS + HS	A_1	753	833			859	IMS + HB
B_2	988	1145				IMS + HB	A_1	868	941	910			IMS + HB
B_2	1162	1273				HB	A_1	1013	1002	1035		1048	HB + IMS
A_1	1372	1340				HB	A_1	1300	1282				HB
B_1	94	117				ET	A_2	88	120				ET
B_1	215	174	152	151	155.8	ET	A_2	216	179	154	159		ET
A_2	103	224				ER	A_2	166	221	206	211		ER
A_2	341	347				IMB	A_2	625	354				IMB
B_1	584	475	475	470	474.5	IMB	A_2	550	467	485	483		IMB
B_1	773	680			564.1	IMB + HS	A_2	672	529				IMB + HS
A_2	641	826				IMS + HS	A_2	751	804				IMS + HB
B_1	975	1021				IMS + HS	A_2	1028	1027	1008			IMS + HB
A_2	742	1104				HS + HB	A_2	2580	2719				HS
B_1	1371	1349				HB	A_2	1301	1282				HB
A_2	1000	1277				HB	A_2	820	957				HB

This classification can be applied to the Γ -point phonon results as well as to the phonon bands obtained from the phonon density of states (DOS) results which are shown below.

The SM results for the chosen Brillouin zone-center phonons are compared in table 3 with the AI (vdW-DF) results and with the available experimental data. A good overall agreement is observed between the SM frequencies and the corresponding AI [22] and experimental data, as well as with other AI phonon calculations for KDP [23]. Despite the fact that we are analysing a hypothetical PE phase at 0 K where the protons are fixed centered in the H-bonds, and that the low frequency phonons and modes involving hydrogen atoms may be affected by the three unstable modes arising from the used approximation, it is instructive to qualitatively compare the changes observed in the phonon spectrum between both PE and FE phases. For instance, one of the unstable modes in the PE phase of B_2 symmetry, which is identified by its imaginary frequency in table 3, corresponds to a similar one found with the AI calculations. Such B_2 mode is the FE soft mode in the PE phase, which becomes stable in the FE phase as a high-frequency HS phonon (see table 3).

When the phase changes from PE to FE some modes soften while others stiffen and, with a few exceptions, the SM phonons follow the same trend as the AI phonons. In particular, one of the most significant frequency changes between both phases is observed for the PO_4 -rotational A_1 mode obtained at 648 cm^{-1} in the PE phase for the SM calculation, which softens to 274 cm^{-1} in the FE phase (see

table 3). Similarly, this mode softens strongly in the AI calculation. It is demonstrated that this phonon couples significantly with the FE soft mode and that this interaction becomes stronger as the amplitude of the latter is increased [22]. The FE soft-mode picture for the phase transition in H-bonded ferroelectrics is consistent with recent NMR experiments which show the importance of a displacive component near the critical temperature [54, 55].

The total SM-DOSs in the FE and PE phases are plotted in figure 1 and compared to the corresponding AI (vdW-DF) results, showing a general good agreement between both calculations for both phases. Notice that the SM and AI (vdW-DF) unstable phonon bands observed in the PE phase at imaginary frequencies (plotted as negative frequencies in the right-hand panel of figure 1), are related to the unstable FE zone-center phonon reported in table 3.

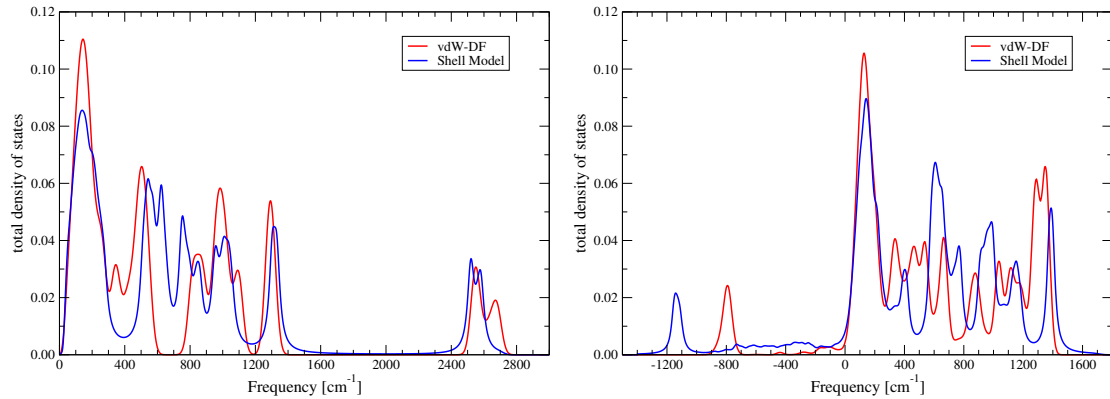


Figure 1. (Colour online) Left-hand panel: SM (blue solid line) and AI (red solid line) results of the total phonon density of states in the FE phase of KDP. Right-hand panel: *idem* for the PE phase. The AI PDOS in the FE phase are results from reference [22].

From these plots and the classification of the phononic displacement patterns made in table 3, we can identify the different types of bands present in the spectra for the FE phase. The highest-frequency band corresponds to the HS band centered at $\approx 2550 \text{ cm}^{-1}$ for the SM calculation which is in very good agreement with the AI result for the HS band centered at $\approx 2600 \text{ cm}^{-1}$ as shown in the left-hand panel of figure 1. Particularly, the bimodal shape of this band and the spectral weight are correctly described by the SM calculation, although the position of the highest-frequency peak of the SM bimodal distribution is a bit shifted towards lower frequencies with respect to the AI result.

The SM result for the HB band is also in remarkable agreement with the corresponding AI result, displaying similar peak positions ($\approx 1300 \text{ cm}^{-1}$) and band extensions in both calculations (see figure 1). The large gap between the HB and HS bands observed in the FE phase in the AI calculation is also qualitatively reproduced by the SM results as shown in figure 1. We also find that the SM DOS result is in qualitative agreement with another AI calculation for the FE phase [38].

The SM lowest-frequency band in the FE phase centered at $\approx 150 \text{ cm}^{-1}$ is also in very good agreement with the corresponding AI data (see figure 1). This is a lattice external (ET+ER) band that extends up to $\approx 300 \text{ cm}^{-1}$, which is of K and O character mainly.

The intermediate frequency region of the DOSs spectra for the FE phase consists of two bands of internal molecular (IM) phonons involving primarily the PO_4 tetrahedron. The high-frequency band extends from ≈ 700 to $\approx 1200 \text{ cm}^{-1}$ in the SM calculation in close agreement with the AI result [22] (see figure 1), and consists of the modes involving mainly the stretching of the P–O bonds (IMS band). The other IM band is observed in the SM calculation in the region $\approx 400\text{--}700 \text{ cm}^{-1}$, and involves the O–P–O bending modes (IMB band) as shown in figure 1. The SM IMB band is associated with two peaks similarly to the AI band, but appears shifted $\approx 150 \text{ cm}^{-1}$ towards higher frequencies than the corresponding AI band. Unfortunately, any attempt to improve the fitting of these bands by modifying different parameters led to a worsening of the overall fit.

Infrared measurements of the imaginary dielectric function at 80 K in KDP with the electric field polarized along the FE axis show well-defined peaks up to $\approx 1400 \text{ cm}^{-1}$ [21]. The main resonances

are: three in the region (0–700) cm^{-1} , centered at ≈ 200 , 300 and 500 cm^{-1} , and the other three in the region (700–1400) cm^{-1} , centered at ≈ 900 , 1000 and 1300 cm^{-1} . These resonances also appear in the infrared spectrum obtained with the electric field polarized in the plane perpendicular to the FE axis [21]. Our SM phononic band structure in the FE phase is in close agreement with the infrared spectra and enables us to identify the main experimental peaks. For instance, the experimental peaks centered at ≈ 200 and 1300 cm^{-1} are in remarkable agreement with the SM lattice external (ET+ER) and HB bands centered at ≈ 150 and 1300 cm^{-1} , respectively. On the other hand, the bands observed experimentally at ≈ 900 and 1000 cm^{-1} can be assigned to our SM bands centered at ≈ 800 and 1000 cm^{-1} which are of IMS+HB character (see the left-hand panel of figure 1 and table 3). The experimental peak observed at $\approx 500 \text{ cm}^{-1}$ should be related to the SM IMB+HB band centered at nearly the same frequency, as shown in the left-hand panel of figure 1. These assignments coincide with those made by the AI calculation of reference [22] (see also the similarities in the band distributions for the SM and AI calculations in the left-hand panel of figure 1). On the other hand, the experimental peak at 300 cm^{-1} can be ascribed to a mixed IMB+lattice band centered at $\approx 250 \text{ cm}^{-1}$ observed in the SM and AI results which mainly involve O, K and P displacements (see the left-hand panel of figure 1), or it can be related to the well-defined AI IMB band centered at $\approx 350 \text{ cm}^{-1}$. Notice that in the latter case, the SM IMB band cannot account for it because it is shifted towards higher frequencies.

3.2.2. Effective Debye temperature

With the aid of the developed model, we have calculated the effective (or equivalent) Debye temperature in the FE phase, $\Theta_D(T)$, as an integral property of the total DOS [22, 35, 56, 57]. This temperature is associated to the value of the specific heat at each temperature [56]. The SM results for $\Theta_D(T)$ are plotted in figure 2 as a function of T and compared to the corresponding AI data of reference [22] and the available experimental data [58–60]. A very good overall agreement of the SM results with the AI and experimental data is obtained, especially at temperatures $\gtrsim 10$ K, as can be judged from figure 2.

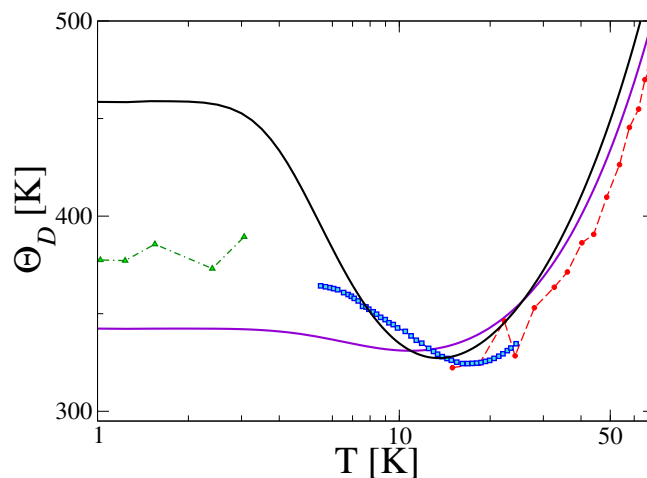


Figure 2. (Colour online) Equivalent Debye temperature $\Theta_D(T)$ as a function of T displayed in logarithmic scale. The theoretical results for the SM and AI calculations are shown in black and magenta solid lines, respectively. The experimental results are plotted with red solid circles and dashed line (reference [58]), with blue open squares (reference [59]), and with green open triangles (reference [60]).

The low-temperature Debye region, where $\Theta_D(T)$ is temperature independent and the Debye model is strictly valid, is observed at $T \lesssim 3$ K and $T \lesssim 4$ K for both SM and AI calculations, respectively. This is in qualitative agreement with the experimental Debye region observed at $T \lesssim 5$ K considering the results of references [59, 60], as shown in figure 2. As $T \rightarrow 0$, $\Theta_D(T)$ takes the value of ≈ 450 K for the SM which is in qualitative agreement with the corresponding experimental and AI values, ≈ 380 K and ≈ 350 K, respectively. The SM curve for $\Theta_D(T)$ reaches a minimum value at ≈ 13 K in very good agreement with the corresponding minima observed in the AI and experimental results, as shown in

figure 2. However, the large drop observed in the SM result for $\Theta_D(T)$ from the Debye region to the minimum value is overestimated in comparison with the corresponding falls in the AI and experimental curves. The observed drop is a typical feature in the effective Debye-temperature profile which is produced by strong hybridizations of the acoustic and low-frequency optical branches towards the Brillouin zone boundary [57].

3.3. Molecular dynamics simulations

Finally we have performed classical-nuclei SMMD and AIMD simulations to study the phase transition in DKDP, which is expected to have less quantum effects than KDP. To track the transition we must first define the order parameter. To accomplish this, we assign to each proton a positive (+) or negative (-) displacement x_i from the instantaneous O–H–O bond center. The values of x_i are considered positive if the proton displacement direction in the particular O–H–O bond i coincides with that observed for the global FE mode which causes polarization in the $z+$ direction, or negative otherwise [22]. It is worth noting here that the coordinated proton displacements around each phosphate following the FE mode pattern are strongly correlated with the local ionic plus electronic polarization along the z direction [7, 16]. The order parameter x is then computed as the spatial and time average of all proton displacements x_i . We define the critical temperature T_c as the temperature at which the order parameter falls to half of its maximum value in the ordered phase.

Figure 3 depicts x vs. T for the AI and SM simulations. Simulations at different temperatures show that the system has a FE ordering up to a critical temperature T_c . For larger temperatures, the average total order parameter vanishes and the PE phase arises. We observe an excellent agreement for the values of T_c obtained with the SMMD and AIMD simulations for DKDP, $T_c^{\text{SM}}(\text{DKDP}) \approx 360$ K and $T_c^{\text{AI}}(\text{DKDP}) \approx 365$ K, respectively. Notice that the present molecular dynamics calculations do not consider the quantum nature of the protons (and hence the possibility of proton tunneling), and for this reason the theoretical values of T_c are expected to be larger than the corresponding experimental value for DKDP, which is $T_c^{\text{exp}}(\text{DKDP}) \approx 229$ K [2, 3].

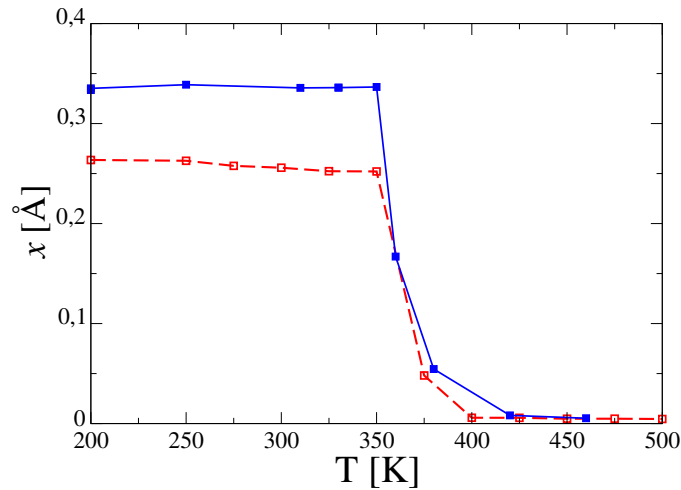


Figure 3. (Colour online) Average order parameter x as a function of T obtained by AIMD and SMMD simulations. We show with red open squares and dashed lines the AIMD results and with blue solid squares and solid lines the SMMD results for DKDP. Lines are guides to the eye only.

4. Summary

We have developed a SM fitted to AI results that include non-local vdW corrections which are important to properly describe H-bond geometries and global proton-transfer energy barriers. The development

of this model is a first step for a future dynamical study in large-size systems of the elusive nature of the ferroelectric phase transition in KDP and other compounds of the H-bonded FE family. The SM was extensively tested by comparing structural and vibrational results to the corresponding first principles and experimental data. The relaxed lattice and atomic structural parameters in the FE and PE phases are in very good correspondence with the respective vdW-corrected AI data as well as with the available experimental data.

Regarding the vibrational properties, the SM Γ -point phonons obtained for the FE and PE phases are in good overall agreement with the corresponding AI results and the available experimental data. The FE mode at the Brillouin zone center calculated with the developed SM is unstable in the PE phase, in agreement with the AI results. The total SM-DOSs in the FE and PE phases are also in very good accordance with the corresponding AI data suggesting that the model represents well the vibrational properties of KDP throughout the whole Brillouin zone. On the other hand, the obtained SM IMB band is in qualitative agreement with the corresponding AI band, but is shifted $\approx 150 \text{ cm}^{-1}$ towards higher frequencies. The SM and AI bands in the FE phase are also in very good agreement with the resonances observed in infrared measurements of the imaginary dielectric function at 80 K in KDP, which enables us to associate the measured peaks with the corresponding phononic displacement patterns. Using the phonon DOS obtained in the FE phase with the developed SM, we have computed the effective Debye temperature which is in very good agreement with the corresponding AI and experimental data. Finally, we have carried out SMMD simulations for classical nuclei and found a FE-PE phase transition for DKDP at $\approx 360 \text{ K}$ which is in very good agreement with the corresponding AIMD simulations that include nonlocal dispersion effects via the vdW-DF approach.

Acknowledgements

We acknowledge support from Consejo Nacional de Investigaciones Científicas y Técnicas (CONICET) and Centro de Simulación Computacional para Aplicaciones Tecnológicas (CSC-CONICET) for the computing hours provided to perform the simulations of this work.

References

1. Lines M. E., Glass A. M., Principles and Applications of Ferroelectric and Related Materials, Clarendon, Oxford, 1977.
2. McMahan M. I., Nelmes R. J., Kuhst W. F., Dorwarth R., Piltz R. O., Tun Z., Nature, 1990, **348**, 317, doi:10.1038/348317a0.
3. Nelmes R. J., McMahan M. I., Piltz R. O., Wright N. G., Ferroelectrics, 1991, **124**, 355, doi:10.1080/00150199108209465.
4. Blinc R., J. Phys. Chem. Solids, 1960, **13**, 204, doi:10.1016/0022-3697(60)90003-2.
5. Reiter G. F., Mayers J., Platzman P., Phys. Rev. Lett., 2002, **89**, 135505, doi:10.1103/PhysRevLett.89.135505.
6. Blinc R., Žekš B., Ferroelectrics, 1987, **72**, 193, doi:10.1080/00150198708017947.
7. Koval S., Kohanoff J., Lasave J., Colizzi G., Migoni R. L., Phys. Rev. B, 2005, **71**, 184102, doi:10.1103/PhysRevB.71.184102.
8. Lasave J., Koval S., Dalal N. S., Migoni R. L., Phys. Rev. Lett., 2007, **98**, 267601, doi:10.1103/PhysRevLett.98.267601.
9. Lasave J., Koval S., Migoni R. L., Dalal N. S., J. Chem. Phys., 2011, **135**, 084504, doi:10.1063/1.3624616.
10. Lasave J., Abufager P., Koval S., Phys. Rev. B, 2016, **93**, 134112, doi:10.1103/PhysRevB.93.134112.
11. Zachek I. R., Shchur Ya., Levitskii R. R., Bilenka O. B., Phys. B, 2014, **452**, 152, doi:10.1016/j.physb.2014.07.020.
12. Zachek I. R., Levitskii R. R., Shchur Ya., Bilenka O. B., Condens. Matter Phys., 2015, **18**, doi:10.5488/CMP.18.43703.
13. Shchur Ya., Bryk T., Klevets I., Kityk A. V., Comput. Mater. Sci., 2016, **111**, 301, doi:10.1016/j.commatsci.2015.09.014.
14. Horiuchi S., Kumai R., Tokura Y., J. Am. Chem. Soc., 2005, **127**, 5010, doi:10.1021/ja042212s.
15. Horiuchi S., Tokunaga Y., Giovannetti G., Picozzi S., Itoh H., Shimano R., Kumai R., Tokura Y., Nature, 2010, **463**, 789, doi:10.1038/nature08731.

16. Koval S., Kohanoff J., Migoni R. L., Tosatti E., Phys. Rev. Lett., 2002, **89**, 187602, doi:10.1103/PhysRevLett.89.187602.
17. Kobayashi K. K., J. Phys. Soc. Jpn., 1968, **24**, 497, doi:10.1143/JPSJ.24.497.
18. Tokunaga M., Matsubara T., Ferroelectrics, 1987, **72**, 175, doi:10.1080/00150198708017946.
19. Sugimoto H., Ikeda S., Phys. Rev. Lett., 1991, **67**, 1306, doi:10.1103/PhysRevLett.67.1306.
20. Merunka D., Rakvin B., Phys. Rev. B, 2002, **66**, 174101, doi:10.1103/PhysRevB.66.174101.
21. Simon P., Gervais F., Courtens E., Phys. Rev. B, 1988, **37**, 1969, doi:10.1103/physrevb.37.1969.
22. Menchón R., Colizzi G., Johnston C., Torresi F., Lasave J., Koval S., Kohanoff J., Migoni R., Phys. Rev. B, 2018, **98**, 104108, doi:10.1103/PhysRevB.98.104108.
23. Shchur Ya., Kityk A. V., Strelchuk V. V., Nikolenko A. S., Andrushchak N. A., Huber P., Andrushchak A. S., J. Alloys Compd., 2021, **868**, 159177, doi:10.1016/j.jallcom.2021.159177.
24. Srinivasan V., Sebastiani D., J. Phys. Chem. C, 2011, **115**, 12631, doi:10.1021/jp202584p.
25. Engel E. A., J. Chem. Phys., 2018, **148**, 144708, doi:10.1063/1.5017480.
26. Shchur Ya., Levitskii R. R., Vlokh O. G., Kityk A. V., Vysochansky Y. M., Grabar A. A., Condens. Matter Phys., 1999, **2**, 93–108, doi:10.5488/CMP.2.1.93.
27. Fujiwara T., J. Phys. Soc. Jpn., 1970, **29**, 1282, doi:10.1143/JPSJ.29.1282.
28. Shchur Ya., Phys. Rev. B, 2006, **74**, 054301, doi:10.1103/PhysRevB.74.054301.
29. Lasave J., Kohanoff J., Migoni R. L., Koval S., Physica B, 2009, **404**, 2736, doi:10.1016/j.physb.2009.06.143.
30. Koval S., Lasave J., Kohanoff J., Migoni R., Ferroelectrics, 2010, **401**, 103, doi:10.1080/00150191003672677.
31. Sepiarsky M., Asthagiri A., Phillpot S. R., Stachiotti M. G., Migoni R. L., Curr. Opin. Solid State Mater. Sci., 2005, **9**, 107, doi:10.1016/j.cossms.2006.05.002.
32. Koval S., Migoni R., Bonadeo H., J. Phys.: Condens. Matter, 1992, **4**, 4759, doi:10.1088/0953-8984/4/20/003.
33. Koval S., Stachiotti M. G., Migoni R. L., Moreno M. S., Mercader R. C., Peltzer y Blancá E. L., Phys. Rev. B, 1996, **54**, 7151, doi:10.1103/PhysRevB.54.7151.
34. Koval S., Burriel R., Stachiotti M. G., Castro M., Migoni R. L., Moreno M. S., Varela A., Rodriguez C. O., Phys. Rev. B, 1999, **60**, 14496, doi:10.1103/PhysRevB.60.14496.
35. Giefers H., Koval S., Wortmann G., Sturhahn W., Alp E. E., Hu M. Y., Phys. Rev. B, 2006, **74**, 094303, doi:10.1103/PhysRevB.74.094303.
36. Casali R. A., Lasave J., Caravaca M. A., Koval S., Ponce C. A., Migoni R. L., J. Phys.: Condens. Matter, 2013, **25**, 135404, doi:10.1088/0953-8984/25/13/135404.
37. Wikfeldt K. T., Michaelides A., J. Chem. Phys., 2014, **140**, 041103, doi:10.1063/1.4862740.
38. Finkelstein Y., Moreh R., Shang S. L., Shchur Ya., Wang Y., Liu Z. K., J. Chem. Phys., 2016, **144**, 054302, doi:10.1063/1.4940730.
39. Gale J. D., J. Chem. Soc., Faraday Trans., 1997, **93**, 629, doi:10.1039/A606455H.
40. Kresse G., Furthmüller J., Comput. Mater. Sci., 1996, **6**, 15, doi:10.1016/0927-0256(96)00008-0.
41. Kresse G., Furthmüller J., Phys. Rev. B, 1996, **54**, 11169, doi:10.1103/physrevb.54.11169.
42. Dion M., Rydberg H., Schröder E., Langreth D. C., Lundqvist B. I., Phys. Rev. Lett., 2004, **92**, 246401, doi:10.1103/PhysRevLett.92.246401.
43. Klimeš J., Bowler D. R., Michaelides A., Phys. Rev. B, 2011, **83**, 195131, doi:10.1103/PhysRevB.83.195131.
44. Román-Pérez G., Soler J. M., Phys. Rev. Lett., 2009, **103**, 096102, doi:10.1103/PhysRevLett.103.096102.
45. Zhang H., Shang S. L., Wang W. Y., Wang Y., Hui X. D., Chen L. Q., Liu, Z. K. Comput. Mater. Sci., 2014, **89**, 242, doi:10.1016/j.commatsci.2014.03.031.
46. Nelmes R. J., Tun Z., Kuhs W. F., Ferroelectrics, 1987, **71**, 125, doi:10.1080/00150198708224833.
47. Koval S., Kohanoff J., Migoni R. L., Bussmann-Holder A., Comput. Mater. Sci., 2001, **22**, 87, doi:10.1016/S0927-0256(01)00172-0.
48. Togo A., Tanaka I., Scr. Mater., 2015, **108**, 1, doi:10.1016/j.scriptamat.2015.07.021.
49. Kresse G., Furthmüller J., Hafner J., Europhys. Lett., 1995, **32**, 729, doi:10.1209/0295-5075/32/9/005.
50. Coignac J. P., Poulet H., J. Phys. (Paris), 1971, **32**, 679, doi:10.1051/jphys:01971003208-9067900.
51. She C. Y., Broberg T. W., Edwards D. F., Phys. Rev. B, 1971, **4**, 1580, doi:10.1103/PhysRevB.4.1580.
52. Serra K. C., Melo F. E. A., Mendes Filho J., Germano F. A., Moreira J. E., Solid State Commun., 1988, **66**, 575, doi:10.1016/0038-1098(88)90211-6.
53. Tominaga Y., Kasahara M., Urabe H., Tatsuzaki I., Solid State Commun., 1983, **47**, 835, doi:10.1016/0038-1098(83)90077-7.
54. Kweon J. J., Fu R., Choi E. S., Dalal N. S., J. Phys.: Condens. Matter, 2017, **29**, 16LT01, doi:10.1088/1361-648X/aa638a.
55. Dalal N., Klymchyov A., Bussmann-Holder A., Phys. Rev. Lett., 1998, **81**, 5924, doi:10.1103/PhysRevLett.81.5924.
56. Brüesch P., Phonons: Theory and Experiments I, Springer-Verlag, Berlin, 1982.

57. Lasave J., Dominguez F., Koval S., Stachiotti M. G., Migoni R. L., J. Phys.: Condens. Matter, 2005, **17**, 7133, doi:10.1088/0953-8984/17/44/006.
58. Stephenson C. C., Hooley J. G., J. Am. Chem. Soc., 1944, **66**, 1397, doi:10.1021/ja01236a054.
59. Lawless W. N., Lawless T. D., Ferroelectrics, 1982, **45**, 149, doi:10.1080/00150198208202009.
60. Foote M. C., Anderson A. C., Ferroelectrics, 1985, **62**, 11, doi:10.1080/00150198508017913.

Оболонкова модель та першопринципні розрахунки коливних, структурних і сегнетоелектричних властивостей KN_2PO_4

Р. Е. Менхон, Ф. Торресі, Х. Ласаве, С. Коваль

Інститут фізики Росаріо, Національний університет Росаріо та Національна рада з науково-технічних досліджень, вул. 27 лютого, 210 Bis, 2000 Росаріо, Аргентина

Розвинено оболонкову модель для дигідрофосфату калію (KDP), яку прив'язано до результатів першопринципних (*ab initio*) обчислень, що враховують нелокальні поправки ван дер Ваальса. Модель ретельно досліджується шляхом порівняння результатів для структурних, коливних і сегнетоелектричних характеристик з результатами першопринципних розрахунків та експериментальними даними. Релаксаційні структурні параметри дуже добре узгоджуються з результатами *ab initio* та з наявними експериментальними даними. Повна густина фононів та їх густина в Γ точці зони Бріллюена у сегнетоелектричній та параелектричній фазах, розраховані в рамках оболонкової моделі, загалом добре узгоджуються з відповідними результатами *ab initio* та експериментальними даними. Також обчислено ефективну температуру Дебая як функцію T , яка добре відповідає результатам *ab initio* та експериментальним даним. Температура фазового переходу "сегнетофаза-парафаза", отримана шляхом класичної молекулярної динаміки для розвинутої оболонкової моделі, складає ≈ 360 К, що чудово узгоджується з результатами першопринципних молекулярно-динамічних розрахунків.

Ключові слова: сегнетоелектрики, водневі зв'язки, фазові переходи, оболонкова модель, метод функціоналу густини